



Title	Post-annealed graphite carbon nitride nanoplates obtained by sugar-assisted exfoliation with improved visible-light photocatalytic performance
Author(s)	Liu, Wei; Yanase, Takashi; Iwasa, Nobuhiro; Mukai, Shin; Iwamura, Shinichiro; Nagahama, Taro; Shimada, Toshihiro
Citation	Journal of colloid and interface science, 567, 369-378 https://doi.org/10.1016/j.jcis.2020.02.031
Issue Date	2020-05-01
Doc URL	http://hdl.handle.net/2115/84423
Rights	©2020. This manuscript version is made available under the CC-BY-NC-ND 4.0 license http://creativecommons.org/licenses/by-nc-nd/4.0/
Rights(URL)	http://creativecommons.org/licenses/by-nc-nd/4.0/
Type	article (author version)
File Information	Liu4final.pdf



[Instructions for use](#)

Post-annealed graphite carbon nitride nanoplates obtained by sugar-assisted exfoliation with improved visible-light photocatalytic performance

Wei Liu, Takashi Yanase, Nobuhiro Iwasa, Shin Mukai, Shinichiro Iwamura, Taro Nagahama,
and Toshihiro Shimada*

Division of Applied Chemistry, Faculty of Engineering, Hokkaido University,
Kita 13 Nishi 8, Kita-Ku, Sapporo, Hokkaido 060-8628, Japan.

*E-mail: shimadat@eng.hokudai.ac.jp

Abstract: Two-dimensional (2D) graphitic carbon nitride ($g\text{-C}_3\text{N}_4$) nanoplates (CNNP) have become a hot research topic in photocatalysis due to their small thickness and large specific surface area that favors charge transport and catalytic surface reactions. However, the wide application of 2D $g\text{-C}_3\text{N}_4$ nanoplates prepared by ordinary methods suffers from increased band gaps with a poor solar harvesting capability caused by the strong quantum confinement effect and reduced conjugation distance. In this paper, a facile approach of exfoliation and the following fast thermal treatment of the bulk $g\text{-C}_3\text{N}_4$ is proposed to obtain a porous few-layered $g\text{-C}_3\text{N}_4$ with nitrogen defects. Due to the preferable crystal, textural, optical and electronic structures, the as-obtained porous CNNP demonstrated a significantly improved photocatalytic activity towards water splitting than the bulk $g\text{-C}_3\text{N}_4$ and even the 3 nm-thick CNNP obtained by sugar-assisted

exfoliation of the bulk g-C₃N₄. The difference in the enhancement factors between the H₂O splitting and organic decomposition has revealed the effect of N defects. This study offers insightful outlooks on the scalable fabrication of a porous few-layered structure with a promoted photocatalytic performance.

Key words: g-C₃N₄ nanoplates; co-grinding; sugar; thermal treatment; photocatalytic activity

1. Introduction

Since Wang and co-workers initially employed graphitic carbon nitride (g-C₃N₄) as a metal-free photocatalyst to photosplit water into H₂, g-C₃N₄ has become an appealing visible-light photocatalyst because of its outstanding properties including low-cost, easy availability, and high physicochemical stability [1,2]. Thanks to these unique advantages, the g-C₃N₄ has demonstrated great potential in photocatalysis, electrocatalysis, smart assemblies, bioimaging and luminescent immunoassay [2-8]. Nevertheless, due to the highly aggregated layers, the pristine g-C₃N₄ suffers from a poor charge carrier behavior and small surface area (10 m² g⁻¹), resulting in a low photocatalytic performance [9-14]. It was reported that the charge carriers are rather localized and confined to the heptazine rings, and thus not readily involved in the photoreactions, which leads to the high exciton-recombination rate [15]. Therefore, several strategies, including doping with exotic atoms, the design of a novel nanostructure, the sensitization with organic dyes, the loading of co-catalyst and the creation of g-C₃N₄ based heterojunctions, are proposed to improve the photocatalytic performance [16-30].

Specifically, two-dimensional (2D) g-C₃N₄ nanoplates prepared from a variety of delamination

methods, including ultrasonic exfoliation in organic solvents, mechanical exfoliation and thermal oxidation exfoliation, have been the focus of photocatalysis because of their high surface area, plentiful exposed active sites, and small charge diffusion distance [19,31-33]. However, the practical application of 2D g-C₃N₄ nanoplates in photocatalysis remains controversial because of their significantly elevated bandgap caused by the strong quantum confinement effect. Therefore, it was rational to improve its visible light harvesting ability with the 2D structure preserved. Available approaches to engineer its band gap included heteroatom-doping (N, S, Br, O, etc) and nitrogen defects control (cyano groups, nitrogen vacancies) [34-39]. For instance, Niu et al. speculated the distinctive effects of nitrogen defects on the extension of light absorption based on the experimental and theoretical studies. The nitrogen defective g-C₃N₄ demonstrated a greatly enhanced photocatalytic activity due to the narrowed band gaps together with more active sites and suppressed charge recombination rate [40]. Currently, a variety of tactics have been proposed for preparation of the nitrogen defective g-C₃N₄, such as thermal polymerization, hydrothermal treatment, and hydrogen reduction [38,41,42]. However, its wide application was hindered by the inevitable safety problems or tedious procedures. Therefore, it was desirable to develop an effective and reliable method to extend the optical response through the construction of nitrogen defects in the g-C₃N₄ nanoplates. Moreover, it was noteworthy that constructing the porous architecture on the g-C₃N₄ framework facilitated the photocatalysis due to the higher specific surface area, improved visible-light harvesting ability by the effective inner reflections as well as the shortened charge diffusion distance [43,44]. Up to now, methods proposed for the synthesis of the porous g-C₃N₄ include template routes, acid treatment, thermal reaction in an atmosphere of

NH₃, and lyophilization assisted procedures [9,45-47].

In this context, a facile method is now proposed to synthesize the porous g-C₃N₄ nanoplates with extended visible-light absorbance by exfoliation and the following fast thermal treatment. The g-C₃N₄ nanoplates were fabricated by a co-grinding exfoliation method in the presence of glucose followed by a short sonication. The as-synthesized g-C₃N₄ nanoplates were then further modified by the rapid thermal treatment at 700 °C for 2 minutes. This approach shows the merits of a low-cost, sustainable and easy operation. As expected, with the unique porous few-layered and repolymerized heptazine rings structure, the products demonstrated impressively enhanced visible-light photocatalytic activities towards water splitting and degradation of rhodamine B (RhB).

2. Experimental details

2.1. Sample preparation

The pristine g-C₃N₄ was synthesized by the pyrolysis of 6 g of dicyandiamide in a covered crucible at 550 °C for 4 h at the heating rate of 2.3 °C/min. The obtained aggregates were ground into powder and labelled GCN.

The few-layered g-C₃N₄ nanoplates were synthesized by the mechanochemical exfoliation of the pristine g-C₃N₄ in the presence of glucose and denoted as m-CNNP. A 0.2 g sample of GCN was mixed with 1 g of glucose and subjected to grinding using a mortar and pestle for 2.5 h at the rotating speed of around 150 rpm. The milled mixture was then dispersed in water and sonicated during 1h, followed by centrifugation at 3000 rpm (Eppendorf Centrifuge 5415R) for 10 minutes to remove thick sheets. Subsequently, the resultant powder was filtered and washed with abundant deionized water to remove excess glucose thoroughly. The samples were obtained by drying in a

freeze-dryer with yields of 40%.

The porous few-layered g-C₃N₄ nanoplates was obtained by fast annealing of m-CNNP as follows. m-CNNP was placed in a crucible, moved to a furnace preheated at 700 °C for 2 minutes in air. The resulting sample after cooling to ambient temperature was labelled m-CNNP700 with the total production yield of 20%.

2.2. Characterization

The X-ray diffraction (XRD) results were acquired using a Rigaku Miniflex diffractometer. X-ray photoelectron spectroscopy (XPS) was performed by a JEOL JPS-9200. Fourier transform infrared (FTIR) spectra were collected by a JASCO FT/IR-4600 spectrometer. Solid-state ¹H and ¹³C cross-polarisation magic angle spinning nuclear magnetic resonance (CP-MAS-NMR) spectra were obtained using an Avance III HD NMR spectrometer (Bruker BioSpin) linked to a cryomagnet. Scanning electron microscopy (SEM) images were acquired by a JEOL JEM-2010. Transmission electron microscopy (TEM) was conducted on FEI Titan3 G2 60-300. The photoluminescence (PL) emission spectra were carried out using a JASCO FP-8000 fluorescence spectrophotometer. N₂ adsorption-desorption isotherms were recorded by a Quantachrome Autosorb-iQ2. UV–vis diffuse reflectance spectra (DRS) were performed by a JASCO V-750 UV-visible spectrometer. Electrochemical impedance spectroscopy (EIS) results were obtained on a 1260/1287, Solartron Analytical electrochemical workstation. The Mott-Schottky plots were conducted in 0.5 M Na₂SO₄ solution at the frequency of 1000 Hz. The transient photocurrent responses of the catalysts deposited on an ITO slice were tested in a three-electrode cell with an aqueous electrolyte of a 0.5 M Na₂SO₄ solution vs Ag/AgCl.

2.3. Photocatalytic Hydrogen Generation Test

The water splitting reactions were accomplished in a sealed glass reactor. Typically, 30 mg samples were added to 28 ml of a triethanolamine (TEOA) solution (10 vol%) with continuous stirring. A 3 wt% Pt as cocatalyst was then positioned on the photocatalyst by *in situ* photodeposition using $\text{H}_2\text{PtCl}_6 \cdot 6\text{H}_2\text{O}$. Prior to the reaction, nitrogen was introduced into the reactor for 30 min. A 150-W Xe lamp with a 400-nm cutoff filter was employed to trigger the photocatalytic reaction. The generated hydrogen was tested by a gas chromatograph within a thermal conductivity detector (TCD). To measure the apparent quantum efficiency (AQE) during the irradiation of monochromatic light (425, 475, 500, 550 and 600 nm), five different band-pass filters were used as the light source to start the photoreactions. The AQE was calculated as follows:

$$\begin{aligned}\text{QE (\%)} &= \frac{\text{number of reacted electrons}}{\text{number of incident photons}} \times 100 \\ &= \frac{\text{number of evolved H}_2 \text{ molecules} \times 2}{\text{number of incident photons}} \times 100\end{aligned}$$

2.4. Photocatalytic RhB Degradation Test

The photocatalytic performance was further assessed by degradation of Rhodamine B (RhB). A 25-mg samples was added to 50 mL of the RhB solution (10 mg/L). Before the photoreaction, the dispersion was sonicated for 20 min, then stirred for 10 min in the dark to establish the adsorption equilibrium. At 20-minute intervals, 3 mL of the solution was collected and centrifuged to purify the supernatant. The absorbance of the supernatant was tested at the wavelength of 553 nm by a UV-Visible spectrometer.

3. Results and discussion

m-CNNP700 was synthesized by the post annealing of the g-C₃N₄ nanoplates prepared by

mechanochemistry exfoliation of the pristine g-C₃N₄ as illustrated in Fig. 1. First, m-CNNP was fabricated by the co-grinding of the pristine GCN and glucose crystals followed by sonication. After exfoliation, the m-CNNP was subjected to fast thermal annealing, thus yielding m-CNNP700. During the whole process, a co-grinding strategy led to the rupture and exfoliation of the pristine GCN aggregations (Fig. S1) into m-CNNP with a much reduced lateral size and thickness, as revealed by SEM (Fig. 2A) and TEM images (Fig. 2C). The carbon nitride nanoplates dispersion showed a good stability in water up to 48 h (Fig. S2). The fast thermal annealing process then induced the repolymerization of the fragments as well as the generation of porous structures in the layers, finally producing the porous m-CNNP700 (Fig. 2B). As shown in Fig. 2D, m-CNNP700 demonstrated a porous few-layered structure with the lateral size of hundreds of nanometers. The pores on the surface of m-CNNP700 were estimated to be around 50–200 nm. Furthermore, two sharp electron diffraction rings, attributed to the (100) and (002) planes, appeared in the selected area electron diffraction (SAED) pattern of m-CNNP700, indicating its polycrystalline nature with a high crystallinity. As displayed in Fig. 3, the thickness of m-CNNP700 was estimated to be about ~5 nm versus that of ~3 nm for m-CNNP (Fig. S3). The unique porous few-layered structure of m-CNNP700 is conducive to generating more active sites for absorbing more reactant molecules in the porous network as well as a faster charge transfer to the surface for the photoreaction, which favors the photocatalysis.

The crystal structures of the as-obtained samples were evaluated based on their XRD patterns, as displayed in Fig. 4A. For the bulk GCN, the typical diffraction peak at 13.1° (100) is attributable to the in-planar structural packing motif and the peak at 27.4° (002) is an indication of the interlayer-stacking

of the heptazine rings [2]. The XRD pattern of m-CNNP700 is similar to that of GCN, indicating that its crystal structures were basically retained. The diffraction peaks of m-CNNP700 showed a significantly decreased intensity with respect to GCN, indicating the effective delamination and reduction in the planar size after the exfoliation-annealing process [48]. It is noteworthy that the intensity of m-CNNP700 slightly increased compared to m-CNNP, suggesting its improved conjugated aromatic system and better crystallinity after the rapid thermal treatment. The FT-IR spectra of GCN, m-CNNP and m-CNNP700 offers more molecule-level structural details, as displayed in Fig. 4B. We can observe the resemblance in the absorption spectra of all three samples, including the characteristic breathing modes of the CN heterocycles at 810 cm^{-1} , the stretching modes of the triazine units in the $1200\text{--}1700\text{ cm}^{-1}$ region and the hydroxyl groups or amine groups in the range of $3000\text{--}3700\text{ cm}^{-1}$ [49]. The similar characteristic peaks of the three samples evidenced that the 2D hexagonal framework of GCN, m-CNNP and m-CNNP700 remained unchanged, which is crucial for the π -delocalized electronic structure to produce and convey charge carriers for the subsequent redox reactions. Moreover, for the m-CNNP700, an additional absorption band appeared at 2178 cm^{-1} , ascribed to the asymmetric stretching vibration of the cyano groups ($\text{C}\equiv\text{N}$) [39]. The formation of $\text{C}\equiv\text{N}$ is probably caused by the breaking of the in-plane C-N bonds during the annealing process. Additionally, the intensity of the N-H peak for m-CNNP700 around $3000\text{--}3300\text{ cm}^{-1}$ displayed obvious reduction in comparison to the other samples. A similar phenomenon also can also be found in other publications [39,49].

XPS measurements were performed to further characterize the surface chemical states and the atomic composition of the samples. As shown in Fig. 5A, the high-resolution C1s spectrum identified the existence of three different peaks, two at 285.1 and 288.2 eV, respectively,

corresponding to the graphitic C=C or adventitious carbon and N=C(-N)₂, and the third at 286.2 eV, which was assigned to the C-NH₂ [39,40]. Comparatively, the bonding energies of carbon species for m-CNNP700 displayed a slight shift (Table. S1), which is a result of the electron redistribution. The high-resolution N1s spectrum of the pristine CN (Fig. 5B) can be deconvoluted into four peaks, three at 398.4, 399.4, 400.7 eV, respectively, ascribed to the sp² C-N=C, N-(C)₃, and amino functional groups, and the fourth centered at 404.2 eV which originated from the charging effects (π excitation) [39,50]. The m-CNNP possessed the same nitrogen species as those of the pristine GCN, and the peak area percentage of the C-N=C to N-(C)₃ experienced a moderate increase from 3.18 (GCN) to 3.76 (m-CNNP). The decreased ratio of N-(C)₃ for the m-CNNP possibly resulted from the fracture of the sp³ N-(C)₃ bonds induced by the grinding exfoliation [51]. In comparison, after the quick thermal modification, the peak area proportion of C-N=C to N-(C)₃ reduced from 3.76 (m-CNNP) to 2.9 (m-CNNP700), implying the presence of two-coordinated nitrogen vacancies in m-CNNP700 [40]. The existence of a nitrogen vacancy was further proved by the increased C/N ratio according to the elemental analysis (Table S2). As a result, the value of the C/N ratio for m-CNNP700 rose to 0.685 from 0.667 for CN. As displayed in the high-resolution O1s spectra (Fig. S4 and Table S1), two main peaks at 533.6 eV and 531.9 eV are observed for the samples, ascribed to the surface adsorbed O₂ and the C-O species, respectively [40]. With respect to the bulk g-C₃N₄, m-CNNP700 showed slightly increased intensity of the C-O peak, which is probably originates from the thermal oxidation in air. The introduction of O atoms in the framework of g-C₃N₄ is beneficial to the extension of light absorption range and the suppression of the charge recombination, thus in favor of the

enhancement of photoactivity [52].

The molecular-level architectures of GCN, m-CNNP and m-CNNP700 were further detected by solid-state ^{13}C and ^1H CP-MAS-NMR. In the ^{13}C NMR spectra (Fig. S5A), two strong peaks emerged at 156.7 and 164.6 ppm for all the samples, assigned to the characteristic C atoms of $\text{N}=\text{C}-\text{N}_2$ and $\text{N}=\text{C}-\text{N}(\text{NH}_x)$ in the heptazine units, respectively [53]. Figure S5B compares the ^1H NMR spectra of the samples. For m-CNNP, two peaks at 0.97 and 4.30 ppm appeared in the NMR spectra, ascribed to $\text{C}-\text{NH}/-\text{NH}_2$ and $\text{HC}=\text{N}$, respectively [54,55]. With respect to the pristine $\text{g}-\text{C}_3\text{N}_4$, the appearance of $\text{C}-\text{NH}/-\text{NH}_2$ in m-CNNP indicates the decreased crystallinity of m-CNNP, which should be due to the breaking of the $\text{sp}^3 \text{N}-\text{C}$ bonds in m-CNNP caused by the sugar-assisted grinding exfoliation. While for m-CNNP700, the $\text{C}-\text{NH}/-\text{NH}_2$ peak couldn't be detected, which suggested that the annealing process resulted in repolymerization of the broken triazine units. The binding energy in the $\text{N}1\text{s}$ XPS spectrum of m-CNNP700 is also evidenced for the occurrence of the repolymerization, the peak of which at 399.3 eV associated with $\text{sp}^3 \text{N}-\text{C}$ sites showed a reduced area ratio with respect to that of m-CNNP (Table S1). The higher content of $\text{HC}=\text{N}$ probably suggested the occurrence of the breaking of the in-plane $\text{C}-\text{N}$ bonds in m-CNNP700, indicating the formation of the disordered m-CNNP700 with more two-coordinated nitrogen vacancies in agreement with the XPS.

The textural properties of the as-obtained three samples were explored using the N_2 adsorption-desorption isotherm tests. The isotherm of the $\text{g}-\text{C}_3\text{N}_4$ is confirmed as a type IV isotherm and displayed the highest N_2 adsorption at high relative pressures (P/P_0), suggesting the mesoporosity of the samples (Fig. 6) [56]. The pore sizes distribution curves could be obtained by using the Barrett-Joyner-

Halenda (BJH) method, which exhibited a broad distribution in the range from 10 to 200 nm for m-CNNP. The pores were probably caused by the lamellar morphology of g-C₃N₄. m-CNNP possessed a much higher surface area (68 m² g⁻¹) with respect to the pristine CN (6.25 m² g⁻¹). After the rapid thermal treatment of m-CNNP, the surface area of m-CNNP700 slightly reduced to 59 m² g⁻¹, implying that the mesoporosity of the product was mostly maintained. m-CNNP700 also possessed a wide pore size distribution between 10 and 200 nm. It is noteworthy that m-CNNP700 displayed more abundant pores than m-CNNP ranging from 70 to 200 nm, which agrees with the SEM results. The high surface area and pore volume are beneficial to the photocatalytic reactions, because more reactive sites could be formed for accommodating the reactants.

The typical optical properties of the as-synthesized products were revealed by DRS and PL characterization. As displayed in Fig. 7A, the absorption edge experienced an obvious blue shift roughly from 450 nm for the pristine GCN to 420 nm of m-CNNP, while the introduction of N defects into g-C₃N₄ by the fast thermal treatment of the m-CNNP remarkably modified the optical properties and light harvesting capacity of the sample. There appears an obvious red shift in the absorption edge after the rapid thermal modification, implying the possible existence of N defects in the m-CNNP700. The bandgaps of the samples can be calculated from the transformed Kubelka–Munk function. As a result, the bandgap of m-CNNP is broadened from 2.77 for GCN to 2.97 eV, which probably resulted from the quantum confinement effect induced by the exfoliated nano-sized m-CNNP [50]. The blue shift of the bandgap in m-CNNP leads to a lower light harvesting capacity, which has an adverse effect on the photocatalytic reactions. After the thermal

modification, the bandgap of m-CNNP700 is narrowed to 2.80 eV, which is associated with the increased cyano groups in the graphitic carbon nitride [39,40]. Additionally, the light absorbance of m-CNNP700 in the region of 450~700 nm obviously enhanced, which originated from the introduction of the interband defect states caused by the nitrogen vacancy [17]. Based on the FTIR, XPS and NMR analyses, it is concluded that the better light harvesting ability and narrowed bandgap resulted from the presence of nitrogen defects.

The PL spectra were further carried out to analyze the separation efficiency of the photoinduced charge carriers. As displayed in Fig. 7B, an evident blue shift of the emission peak from 475 nm for CN to 450 nm for m-CNNP can be observed, which is in accordance with the absorption spectrum, while after modification by the rapid thermal treatment, the emission PL peak obviously showed a reduced intensity accompanied by a red shift to 480 nm for m-CNNP750, indicating the greatly suppressed charge recombination rate because of the enhanced charge diffusion in the porous few-layered structure. The lower intensity of the PL spectrum reflected the electron relocalization on the surface terminal sites, which is beneficial to the promotion of the photocatalytic performance [57].

The photoelectrochemical tests for the samples were conducted to assess the capacity of the charge shuttling and conveyance to the surface active sites. Figure 7C displays the prompt and persistent photocurrent signals for four continuously on-off illumination cycles. m-CNNP700 exhibits a higher photocurrent intensity than the other two samples, revealing its superior charge separation efficiency. Additionally, as displayed in Fig. 7D, the Nyquist plot of m-CNNP700 had the smallest semicircle diameter with respect to the other samples, implying a much lower charge-

transfer resistance, and thus higher charge transfer efficiency at the solid/liquid interface [58]. Compared to the other samples, the advantageous charge behavior of m-CNNP700 showed the introduction of nitrogen defects and the porous few-layered structure is beneficial to the promotion of the charge separation and transfer.

Furthermore, the valence band (VB) XPS spectra and Mott–Schottky plots were performed to explore the influence of the nitrogen defects on the VB maximum and conduction band minimum (CBM) of the m-CNNP700. All the samples are n-type semiconductors, as revealed by the Mott–Schottky plots (Fig. S6). The flat-band potentials are -0.75, -0.99 and -0.90 eV (vs. NHE, pH = 7) for the GCN, m-CNNP and m-CNNP700, respectively, while the VBM of GCN, m-CNNP and m-CNNP750 are estimated to be 1.99, 1.99 and 1.90 eV, respectively (Fig. 8A). In addition, due to the existence of nitrogen vacancies, the additional electrons would be redistributed to their nearest carbon atoms and delocalized within the π bonds of the g-C₃N₄, thus leading to the vacancy-related state (-0.11 eV) below the CBM of the m-CNNP700 [17,39]. Based on the above-mentioned analysis, a band structure comparison among the GCN, m-CNNP and m-CNNP700 is described in Fig. 8B.

The photocatalytic activities of the pristine CN, m-CNNP and m-CNNP700 samples for water splitting were tested under the visible-light irradiation (>400 nm). As displayed in Fig. 9A, the pristine GCN showed a small photocatalytic H₂-evolution rate of 37.7 $\mu\text{mol h}^{-1} \text{g}^{-1}$, and its exfoliation into the few-layered m-CNNP resulted in the H₂-evolution rate up to 96.7 $\mu\text{mol h}^{-1} \text{g}^{-1}$. The photocatalytic H₂-production rate of m-CNNP700 obtained by the exfoliation-annealing treatment achieved 264.3 $\mu\text{mol h}^{-1} \text{g}^{-1}$, which is higher than that of the pristine GCN and m-CNNP

by about 7-times and 3-times, respectively, confirming the post-thermal treatment of m-CNNP as a valid technique to enhance the hydrogen production. Additionally, m-CNNP700 exhibited a photocatalytic H₂ evolution without any obvious decline during four cycles, validating its good stability for photocatalysis (Fig. 9B). The apparent quantum efficiency (AQE) of m-CNNP was tested to explore the wavelength dependence of the photocatalytic activity in the range of 400–600 nm. As shown in Fig. 9C, the AQE displayed a shape resemblance to the optical absorption spectrum of m-CNNP700 in the visible-light region and the value of AQE at 425 nm was calculated to be 1.0%. This revealed that the H₂ production reaction is driven by photon absorption. The XRD pattern and FTIR spectra further showed that the structure of m-CNNP700 was largely preserved after several reaction cycles (Fig. S7).

The photocatalytic performance of the samples was further tested by the degradation of RhB by visible light excitation. As displayed in Fig. 10A, m-CNNP700 also displayed a good RhB degradation efficiency after a 120-minute illumination. In contrast, only 17% of the RhB can be degraded by the pristine GCN under identical conditions, indicating its very low photodegradation efficiency. After exfoliation of the bulk GCN into a few-layered m-CNNP with a much higher surface area, the RhB degradation efficiency experienced a remarkable increase and 92% of the RhB can be removed after the 120-minute irradiation. After annealing the few-layered m-CNNP at 700 °C for 2 minutes, the produced m-CNNP700 maintained a good RhB degradation efficiency despite the lower surface area and 82% of the RhB was eliminated. Moreover, the photodegradation efficiency of m-CNNP700 did not show a remarkable decrease after 4 cycles, implying its good stability (Fig. S8). Furthermore, the pseudo-first-order model was used to fit the photocatalytic

data in order to study the photocatalytic degradation kinetics. As shown in Fig. 10B, the rate constant of the m-CNNP700 achieved 0.0120 min^{-1} , which outperformed that of GCN (0.0011 min^{-1}) by 11 times and very close to that of m-CNNP (0.0185 min^{-1}) for the RhB degradation, respectively.

The considerable improvement in the photocatalytic activities regarding photosplitting of water for hydrogen and RhB degradation by m-CNNP700 can be understood by multiple rationales. As displayed in Fig. 10C, first, m-CNNP700 features a porous structure with a much reduced thickness, which can provide a high specific surface area to accommodate active sites for the H^+ /TEOA reactants and favor the prompt transport of H^+ /TEOA through the porous architecture. Second, the red-shift of the absorption spectrum upon the introduction of defects endow m-CNNP700 with the capacity to absorb more photons for the photocatalytic activity based on the DRS results (Fig. 7A). The porous structure of m-CNNP can also enhance the light harvesting by the inner light reflection, thus beneficial to the photocatalytic activities. Third, the defect states can act as separation centers to trap photogenerated electrons from the CB and hence speed up the charge separation. Moreover, it is noteworthy that a higher degree of crystallinity for m-CNNP700 is more favorable for the uphill reactions of water splitting due to the presence of fewer recombination centers [59]. While the surface area becomes more important for the photodegradation of organic pollutants because the critical process is adsorption of the RhB molecules, leading to the advantageous degradation efficiency of m-CNNP [60,61]. Consequently, an impressively enhanced photocatalytic performance is acquired owing to the combination effects of the tailored crystal, textural, optical and electronic structures.

4. Conclusion

In summary, we have developed a facile and scalable method to synthesize the porous few-layered g-C₃N₄ material with N defects, via the exfoliation followed by fast thermal treatment of the bulk g-C₃N₄. The m-CNNP700 possessed an expanded visible-light absorption region, enhanced surface area, shortened charge transport distance and promoted charge mobility, originating from its nitrogen-defective and porous few-layered architecture. As expected, the m-CNNP700 materials displayed a 7-fold enhancement in the photocatalytic hydrogen evolution than the pristine g-C₃N₄ and 3-fold greater than that of m-CNNP by visible light irradiation. Our study offered a new tactic for the facile and scalable synthesis of the porous few-layered CNNP for an enhanced photocatalytic performance.

Acknowledgements

The authors are grateful to Professors H. Habazaki, C. Y. Zhu, M. Higuchi, Y. Masubuchi, K. Tadanaga, A. Miura, C. Rosero-Navaro and Ms. Ning Wang for their valuable discussions and experimental facilities. The present research was partly supported by KAKENHI (17H03380) from MEXT, Japan. The instrumental analyses were supported by the Nanotechnology Platform at Hokkaido University by METI, Japan. W.L. thanks the fellowship from the China Scholarship Council (201706950010).

Appendix A. Supporting information

Figures S1–S8, Table S1,S2

Notes

The authors declare no competing financial interest.

References

- [1] Y. Wang, X. Wang, M. Antonietti, Polymeric graphitic carbon nitride as a heterogeneous organocatalyst: from photochemistry to multipurpose catalysis to sustainable chemistry, *Angew. Chem. Int. Ed.* 51 (2012) 68-89.
- [2] X. Wang, K. Maeda, A. Thomas, K. Takane, G. Xin, J.M. Carlsson, K. Domen, M. Antonietti, A metal-free polymeric photocatalyst for hydrogen production from water under visible light, *Nat. Mater.* 8 (2009) 76.
- [3] J. Xu, T.J. Brenner, L. Chabanne, D. Neher, M. Antonietti, M. Shalom, Liquid-based growth of polymeric carbon nitride layers and their use in a mesostructured polymer solar cell with V_{oc} exceeding 1 V, *J. Am. Chem. Soc.* 136 (2014) 13486-13489.
- [4] J. Liu, Y. Liu, N. Liu, Y. Han, X. Zhang, H. Huang, Y. Lifshitz, S.-T. Lee, J. Zhong, Z. Kang, Metal-free efficient photocatalyst for stable visible water splitting via a two-electron pathway, *Science* 347 (2015) 970-974.
- [5] Z. Pei, J. Gu, Y. Wang, Z. Tang, Z. Liu, Y. Huang, Y. Huang, J. Zhao, Z. Chen, C. Zhi, Component matters: paving the roadmap toward enhanced electrocatalytic performance of graphitic C_3N_4 -based catalysts via atomic tuning, *ACS nano* 11 (2017) 6004-6014.
- [6] Y. Zhang, Z. Zhou, Y. Shen, Q. Zhou, J. Wang, A. Liu, S. Liu, Y. Zhang, Reversible assembly of graphitic carbon nitride 3D network for highly selective dyes absorption and regeneration, *ACS nano* 10 (2016) 9036-9043.
- [7] X. Zhang, X. Xie, H. Wang, J. Zhang, B. Pan, Y. Xie, Enhanced photoresponsive ultrathin

- graphitic-phase C₃N₄ nanosheets for bioimaging, *J. Am. Chem. Soc.* 135 (2012) 18-21.
- [8] Q. Wang, W. Wang, J. Lei, N. Xu, F. Gao, H. Ju, Fluorescence quenching of carbon nitride nanosheet through its interaction with DNA for versatile fluorescence sensing, *Anal. Chem.* 85 (2013) 12182-12188.
- [9] Q. Liang, Z. Li, Z.H. Huang, F. Kang, Q.H. Yang, Holey graphitic carbon nitride nanosheets with carbon vacancies for highly improved photocatalytic hydrogen production, *Adv. Funct. Mater.* 25 (2015) 6885-6892.
- [10] J. Zhang, Y. Chen, X. Wang, Two-dimensional covalent carbon nitride nanosheets: synthesis, functionalization, and applications, *Energy Environ. Sci.* 8 (2015) 3092-3108.
- [11] A. Akhundi, A. Habibi-Yangjeh, M. Abitorabi, S. Rahim Pouran, Review on photocatalytic conversion of carbon dioxide to value-added compounds and renewable fuels by graphitic carbon nitride-based photocatalysts, *Catal. Rev.* 61 (2019) 595-628.
- [12] M. Shekofteh-Gohari, A. Habibi-Yangjeh, M. Abitorabi, A. Rouhi, Magnetically separable nanocomposites based on ZnO and their applications in photocatalytic processes: a review, *Crit. Rev. Env. Sci. Tec.* 48 (2018) 806-857.
- [13] M. Pirhashemi, A. Habibi-Yangjeh, S.R. Pouran, Review on the criteria anticipated for the fabrication of highly efficient ZnO-based visible-light-driven photocatalysts, *J. Ind. Eng. Chem.* 62 (2018) 1-25.
- [14] M. Mousavi, A. Habibi-Yangjeh, S.R. Pouran, Review on magnetically separable graphitic carbon nitride-based nanocomposites as promising visible-light-driven photocatalysts, *J. Mater. Sci.: Mater Electron.* 29 (2018) 1719-1747.

- [15] C. Merschjann, T. Tyborski, S. Orthmann, F. Yang, K. Schwarzburg, M. Lublow, M.-C. Lux-Steiner, T. Schedel-Niedrig, Photophysics of polymeric carbon nitride: an optical quasimonomer, *Phys. Rev. B* 87 (2013) 205204.
- [16] Z. Zhao, G. Ge, D. Zhang, Heteroatom-doped carbonaceous photocatalysts for solar fuel production and environmental remediation, *ChemCatChem* 10 (2018) 62-123.
- [17] J. Ran, T.Y. Ma, G. Gao, X.-W. Du, S.Z. Qiao, Porous P-doped graphitic carbon nitride nanosheets for synergistically enhanced visible-light photocatalytic H₂ production, *Energy Environ. Sci.* 8 (2015) 3708-3717.
- [18] W. Liu, N. Iwasa, S. Fujita, H. Koizumi, M. Yamaguchi, T. Shimada, Porous graphitic carbon nitride nanoplates obtained by a combined exfoliation strategy for enhanced visible light photocatalytic activity, *Appl. Surf. Sci.* 499 (2020) 143901.
- [19] P. Niu, L. Zhang, G. Liu, H.M. Cheng, Graphene-like carbon nitride nanosheets for improved photocatalytic activities, *Adv. Funct. Mater.* 22 (2012) 4763-4770.
- [20] D. Chen, K. Wang, W. Hong, R. Zong, W. Yao, Y. Zhu, Visible light photoactivity enhancement via CuTCPP hybridized g-C₃N₄ nanocomposite, *Appl. Catal. B* 166 (2015) 366-373.
- [21] L. Yao, D. Wei, Y. Ni, D. Yan, C. Hu, Surface localization of CdZnS quantum dots onto 2D g-C₃N₄ ultrathin microribbons: highly efficient visible light-induced H₂-generation, *Nano Energy* 26 (2016) 248-256.
- [22] A. Habibi-Yangjeh, M. Mousavi, Deposition of CuWO₄ nanoparticles over g-C₃N₄/Fe₃O₄ nanocomposite: Novel magnetic photocatalysts with drastically enhanced performance under

- visible-light, *Adv. Powder Technol.* 29 (2018) 1379-1392.
- [23] S. Asadzadeh-Khaneghah, A. Habibi-Yangjeh, D. Seifzadeh, Graphitic carbon nitride nanosheets coupled with carbon dots and BiOI nanoparticles: Boosting visible-light-driven photocatalytic activity, *J. Taiwan Inst. Chem. Eng.* 87 (2018) 98-111.
- [24] M. Mousavi, A. Habibi-Yangjeh, Magnetically recoverable highly efficient visible-light-active g-C₃N₄/Fe₃O₄/Ag₂WO₄/AgBr nanocomposites for photocatalytic degradations of environmental pollutants, *Adv. Powder Technol.* 29 (2018) 94-105.
- [25] E. Vesali-Kermani, A. Habibi-Yangjeh, H. Diarmand-Khalilabad, S. Ghosh, Nitrogen photofixation ability of g-C₃N₄ nanosheets/Bi₂MoO₆ heterojunction photocatalyst under visible-light illumination, *J. Colloid Interf. Sci.* 563 (2020) 81–91
- [26] A. Habibi-Yangjeh, M. Mousavi, K. Nakata, Boosting visible-light photocatalytic performance of g-C₃N₄/Fe₃O₄ anchored with CoMoO₄ nanoparticles: Novel magnetically recoverable photocatalysts, *J Photochem. Photobiol. A: Chem.* 368 (2019) 120-136.
- [27] E. Liu, J. Chen, Y. Ma, J. Feng, J. Jia, J. Fan, X. Hu, Fabrication of 2D SnS₂/g-C₃N₄ heterojunction with enhanced H₂ evolution during photocatalytic water splitting, *J. Colloid Interf. Sci.* 524 (2018) 313-324.
- [28] Y. Tian, L. Zhou, Q. Zhu, J. Lei, L. Wang, J. Zhang, Y. Liu, Hierarchical macro-mesoporous g-C₃N₄ with an inverse opal structure and vacancies for high-efficiency solar energy conversion and environmental remediation, *Nanoscale* 11 (2019) 20638-20647.
- [29] H. Dong, M. Xiao, S. Yu, H. Wu, Y. Wang, J. Sun, G. Chen, C. Li, Insight into the Activity and Stability of rhxP Nano-Species Supported on g-C₃N₄ for Photocatalytic H₂ Production,

ACS Catal. 10 (2020) 458–462

- [30] Y. Xu, F. Ge, Z. Chen, S. Huang, W. Wei, M. Xie, H. Xu, H. Li, One-step synthesis of Fe-doped surface-alkalinized g-C₃N₄ and their improved visible-light photocatalytic performance, *Appl. Surf. Sci.* 469 (2019) 739-746.
- [31] M.J. Bojdys, N. Severin, J.P. Rabe, A.I. Cooper, A. Thomas, M. Antonietti, Exfoliation of crystalline 2D carbon nitride: thin sheets, scrolls and bundles via mechanical and chemical routes, *Macromol. Rapid Commun.* 34 (2013) 850-854.
- [32] X. She, H. Xu, Y. Xu, J. Yan, J. Xia, L. Xu, Y. Song, Y. Jiang, Q. Zhang, H. Li, Exfoliated graphene-like carbon nitride in organic solvents: enhanced photocatalytic activity and highly selective and sensitive sensor for the detection of trace amounts of Cu²⁺, *J. Mater. Chem. A* 2 (2014) 2563-2570.
- [33] Y. Yang, L. Geng, Y. Guo, J. Meng, Y. Guo, Easy dispersion and excellent visible-light photocatalytic activity of the ultrathin urea-derived g-C₃N₄ nanosheets, *Appl. Surf. Sci.* 425 (2017) 535-546.
- [34] J. Fang, H. Fan, M. Li, C. Long, Nitrogen self-doped graphitic carbon nitride as efficient visible light photocatalyst for hydrogen evolution, *J. Mater. Chem. A* 3 (2015) 13819-13826.
- [35] G. Liu, P. Niu, C. Sun, S.C. Smith, Z. Chen, G.Q. Lu, H.-M. Cheng, Unique electronic structure induced high photoreactivity of sulfur-doped graphitic C₃N₄, *J. Am. Chem. Soc.* 132 (2010) 11642-11648.
- [36] Z.-A. Lan, G. Zhang, X. Wang, A facile synthesis of Br-modified g-C₃N₄ semiconductors for photoredox water splitting, *Appl. Catal. B* 192 (2016) 116-125.

- [37] J. Li, B. Shen, Z. Hong, B. Lin, B. Gao, Y. Chen, A facile approach to synthesize novel oxygen-doped g-C₃N₄ with superior visible-light photoreactivity, *Chem. Commun.* 48 (2012) 12017-12019.
- [38] P. Niu, G. Liu, H.-M. Cheng, Nitrogen vacancy-promoted photocatalytic activity of graphitic carbon nitride, *J. Phys. Chem. C* 116 (2012) 11013-11018.
- [39] H. Yu, R. Shi, Y. Zhao, T. Bian, Y. Zhao, C. Zhou, G.I. Waterhouse, L.Z. Wu, C.H. Tung, T. Zhang, Alkali-assisted synthesis of nitrogen deficient graphitic carbon nitride with tunable band Structures for efficient visible-light-driven hydrogen evolution, *Adv. Mater.* 29 (2017) 1605148.
- [40] P. Niu, M. Qiao, Y. Li, L. Huang, T. Zhai, Distinctive defects engineering in graphitic carbon nitride for greatly extended visible light photocatalytic hydrogen evolution, *Nano Energy* 44 (2018) 73-81.
- [41] Z. Hong, B. Shen, Y. Chen, B. Lin, B. Gao, Enhancement of photocatalytic H₂ evolution over nitrogen-deficient graphitic carbon nitride, *J. Mater. Chem. A* 1 (2013) 11754-11761.
- [42] P. Niu, L.C. Yin, Y.Q. Yang, G. Liu, H.M. Cheng, Increasing the visible light absorption of graphitic carbon nitride (Melon) photocatalysts by homogeneous self-modification with nitrogen vacancies, *Adv. Mater.* 26 (2014) 8046-8052.
- [43] J. Fu, B. Zhu, C. Jiang, B. Cheng, W. You, J. Yu, Hierarchical porous O-doped g-C₃N₄ with enhanced photocatalytic CO₂ reduction activity, *Small* 13 (2017) 1603938.
- [44] J. Wen, J. Xie, X. Chen, X. Li, A review on g-C₃N₄-based photocatalysts, *Appl. Surf. Sci.* 391 (2017) 72-123.

- [45] J. Zhang, F. Guo, X. Wang, An optimized and general synthetic strategy for fabrication of polymeric carbon nitride nanoarchitectures, *Adv. Funct. Mater.* 23 (2013) 3008-3014.
- [46] L. Shi, K. Chang, H. Zhang, X. Hai, L. Yang, T. Wang, J. Ye, Drastic Enhancement of Photocatalytic Activities over Phosphoric Acid Protonated Porous g-C₃N₄ Nanosheets under Visible Light, *Small* 12 (2016) 4431-4439.
- [47] Q. Han, B. Wang, Y. Zhao, C. Hu, L. Qu, A graphitic-C₃N₄ “seaweed” architecture for enhanced hydrogen evolution, *Angew. Chem.* 127 (2015) 11595-11599.
- [48] Q. Han, C. Hu, F. Zhao, Z. Zhang, N. Chen, L. Qu, One-step preparation of iodine-doped graphitic carbon nitride nanosheets as efficient photocatalysts for visible light water splitting, *J. Mater. Chem. A* 3 (2015) 4612-4619.
- [49] D. Zhang, Y. Guo, Z. Zhao, Porous defect-modified graphitic carbon nitride via a facile one-step approach with significantly enhanced photocatalytic hydrogen evolution under visible light irradiation, *Appl. Catal. B* 226 (2018) 1-9.
- [50] S. Yang, Y. Gong, J. Zhang, L. Zhan, L. Ma, Z. Fang, R. Vajtai, X. Wang, P.M. Ajayan, Exfoliated graphitic carbon nitride nanosheets as efficient catalysts for hydrogen evolution under visible light, *Adv. Mater.* 25 (2013) 2452-2456.
- [51] Q. Han, F. Zhao, C. Hu, L. Lv, Z. Zhang, N. Chen, L. Qu, Facile production of ultrathin graphitic carbon nitride nanoplatelets for efficient visible-light water splitting, *Nano Res.* 8 (2015) 1718-1728.
- [52] L. Yang, J. Huang, L. Shi, L. Cao, Q. Yu, Y. Jie, J. Fei, H. Ouyang, J. Ye, A surface modification resultant thermally oxidized porous g-C₃N₄ with enhanced photocatalytic

- hydrogen production, *Appl. Catal. B: Environ.* 204 (2017) 335-345.
- [53] G. Zhang, C. Huang, X. Wang, Dispersing molecular cobalt in graphitic carbon nitride frameworks for photocatalytic water oxidation, *Small* 11 (2015) 1215-1221.
- [54] K. Schwinghammer, M.B. Mesch, V. Duppel, C. Ziegler, J.r. Senker, B.V. Lotsch, Crystalline carbon nitride nanosheets for improved visible-light hydrogen evolution, *J. Am. Chem. Soc.* 136 (2014) 1730-1733.
- [55] D. Zhao, J. Chen, C.-L. Dong, W. Zhou, Y.-C. Huang, S.S. Mao, L. Guo, S. Shen, Interlayer interaction in ultrathin nanosheets of graphitic carbon nitride for efficient photocatalytic hydrogen evolution, *J. Catal.* 352 (2017) 491-497.
- [56] J. Yuan, J. Wen, Y. Zhong, X. Li, Y. Fang, S. Zhang, W. Liu, Enhanced photocatalytic H₂ evolution over noble-metal-free NiS cocatalyst modified CdS nanorods/g-C₃N₄ heterojunctions, *J. Mater. Chem. A* 3 (2015) 18244-18255.
- [57] B. Long, J. Lin, X. Wang, Thermally-induced desulfurization and conversion of guanidine thiocyanate into graphitic carbon nitride catalysts for hydrogen photosynthesis, *J. Mater. Chem. A* 2 (2014) 2942-2951.
- [58] M.Z. Rahman, J. Ran, Y. Tang, M. Jaroniec, S.Z. Qiao, Surface activated carbon nitride nanosheets with optimized electro-optical properties for highly efficient photocatalytic hydrogen production, *J. Mater. Chem. A* 4 (2016) 2445-2452.
- [59] G. Liu, G. Zhao, W. Zhou, Y. Liu, H. Pang, H. Zhang, D. Hao, X. Meng, P. Li, T. Kako, In Situ Bond Modulation of Graphitic Carbon Nitride to Construct p-n Homojunctions for Enhanced Photocatalytic Hydrogen Production, *Adv. Funct. Mater.* 26 (2016) 6822-6829.

- [60] A. Kudo, Y. Miseki, Heterogeneous photocatalyst materials for water splitting, *Chem. Soc. Rev.* 38 (2009), 253–278.
- [61] P. Niu, H. Li, Y. Ma, T. Zhai, Extended visible light absorption combined with promoted charge carrier transfer in urea-derived graphitic carbon nitride for enhanced photocatalytic hydrogen evolution performances, *J. Phys. Chem. C* 122 (2018), 20717-20726.

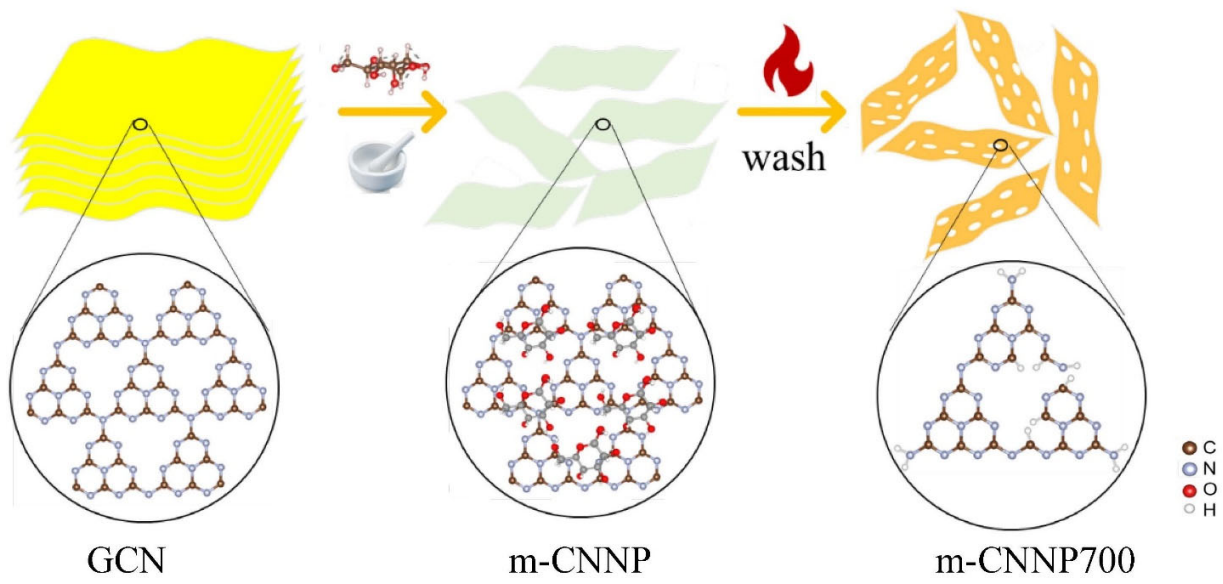


Fig.1 Illustration of the exfoliation procedure

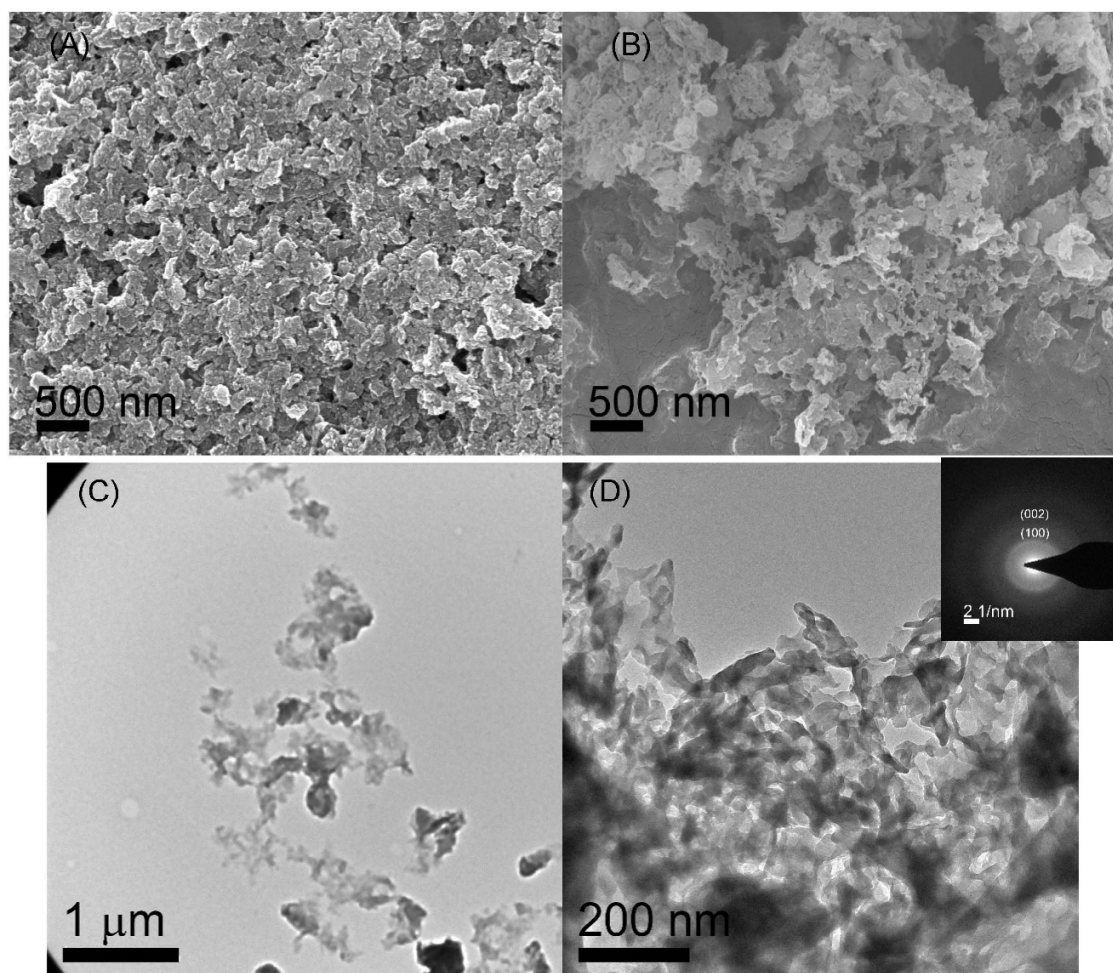


Fig. 2 Typical SEM of the as-synthesized (A) m-CNNP and (B) m-CNNP700. TEM images of as-synthesized (C) m-CNNP and (D) m-CNNP700. Inset shows the SEAD pattern of m-CNNP700.

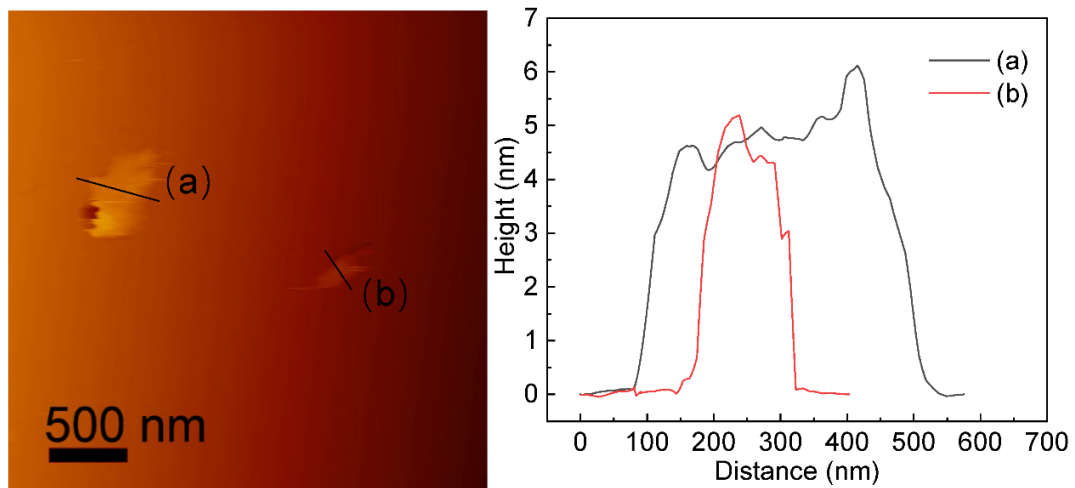


Fig. 3 (A) AFM image of m-CNNP700 on the Si substrate (B) Height profile along the line in (A)

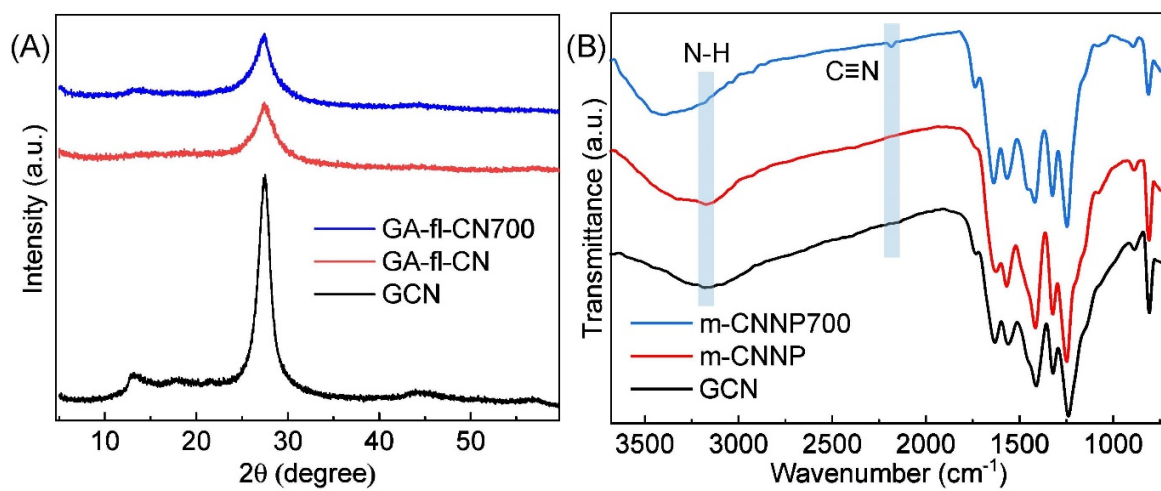


Fig. 4 (a) XRD patterns and (b) FT-IR of the as-prepared GCN, m-CNNP and m-CNNP700

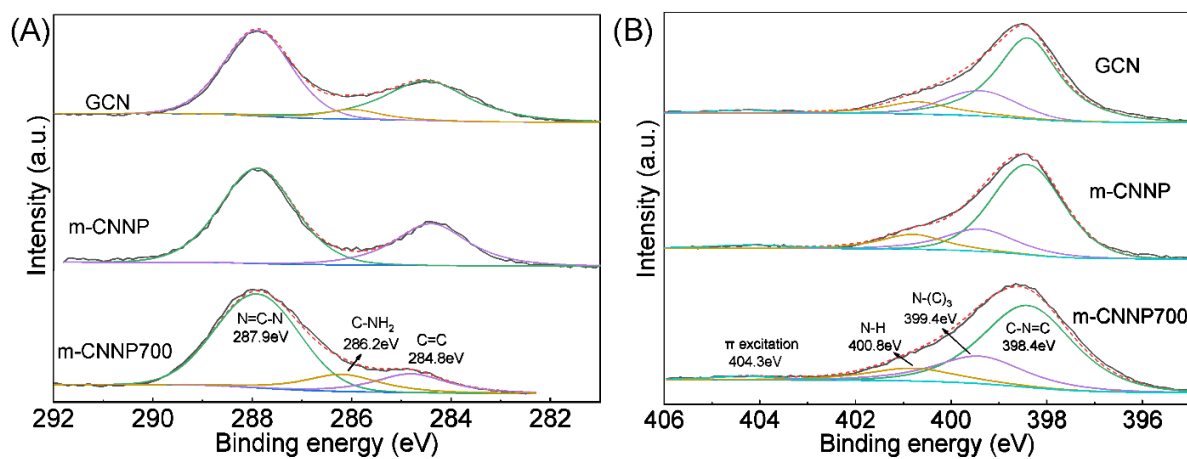


Fig. 5 High-resolution (A) C1s and (B) N1s XPS spectra of the as-synthesized GCN, m-CNNP and m-CNNP700

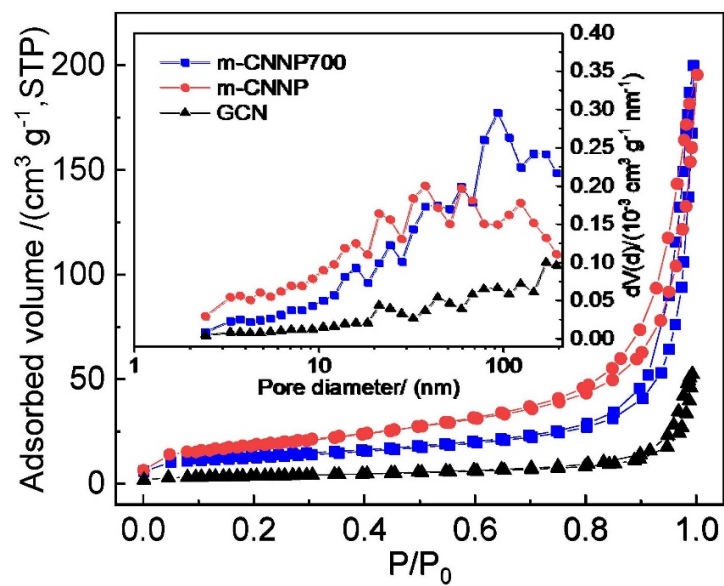


Fig. 6 N_2 adsorption/desorption isotherms of the as-synthesized GCN, m-CNNP and m-CNNP700. The inset is the corresponding pore size distribution plots

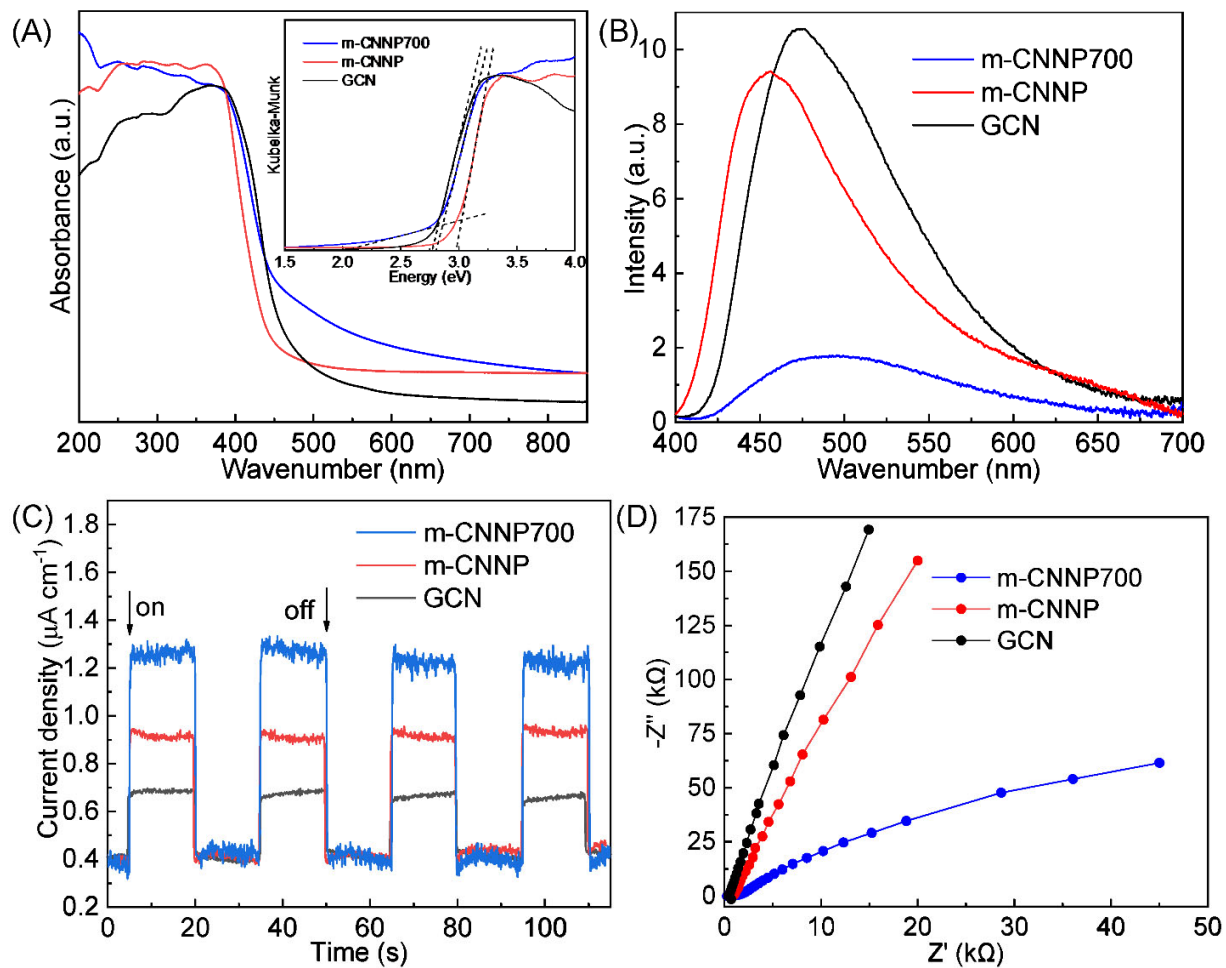


Fig. 7 (A) UV-vis absorption spectra, (B) PL emission spectra, (C) transient photocurrent spectra and (D) Nyquist plots of EIS of the as-synthesized GCN, m-CNNP and m-CNNP700

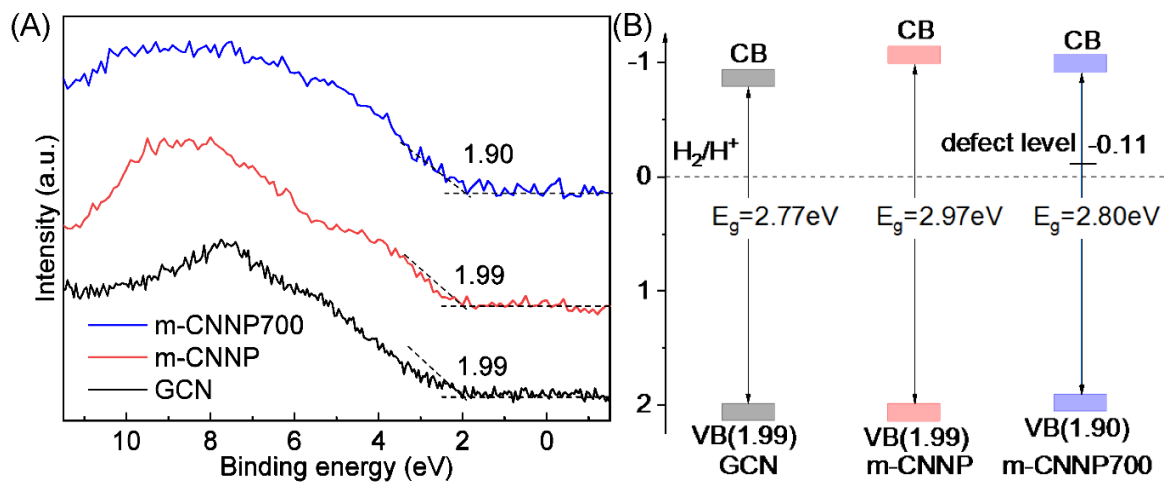


Fig. 8 (A) XPS valence band spectra and (B) electronic band illustration of the as-fabricated GCN, m-CNNP and m-CNNP700.

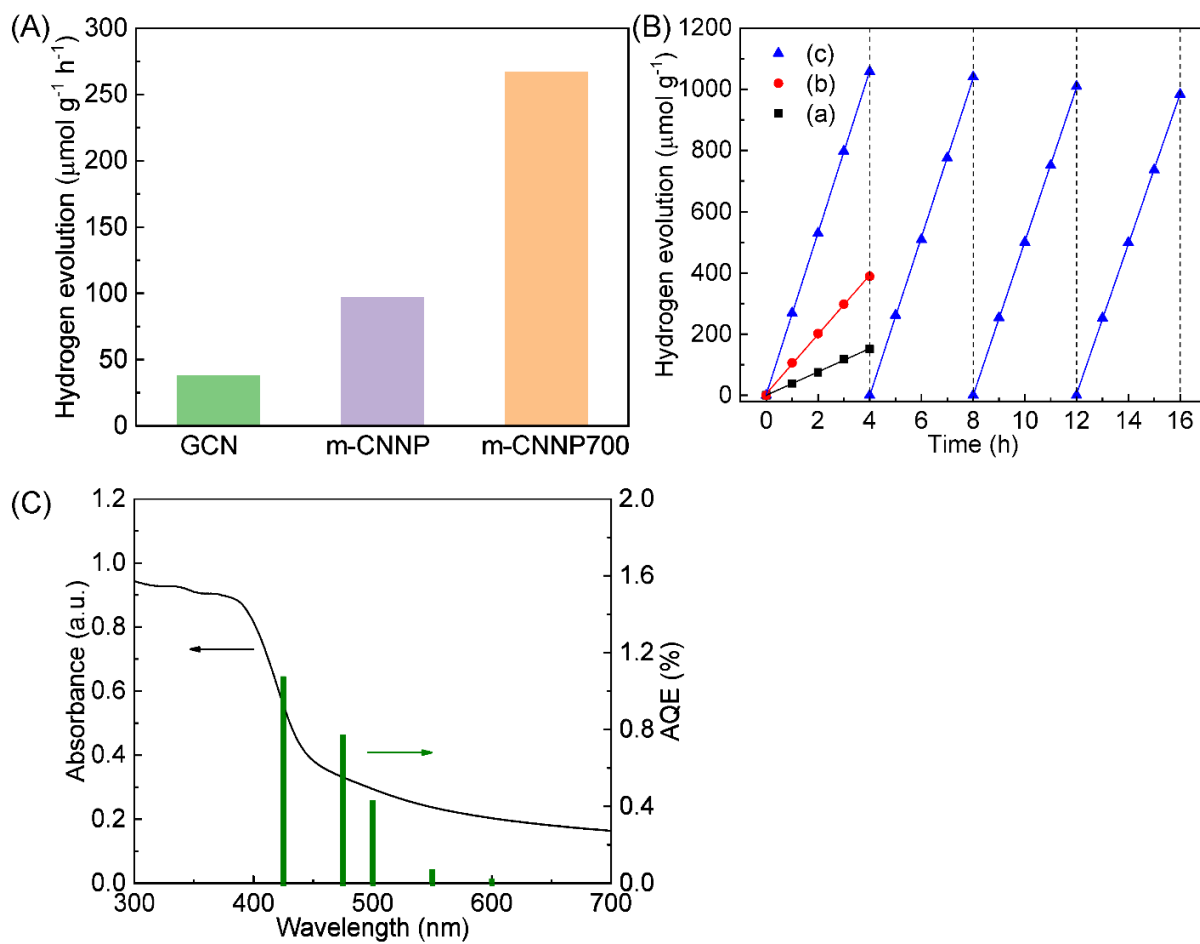


Fig. 9 (A) Hydrogen evolution rate, (B) test for the stability of hydrogen evolution over the as-fabricated (a) GCN, (b) m-CNNP and (c) m-CNNP700. (C) AQE of m-CNNP700 at 425 nm, 475 nm, 500 nm, 550 nm and 600 nm.

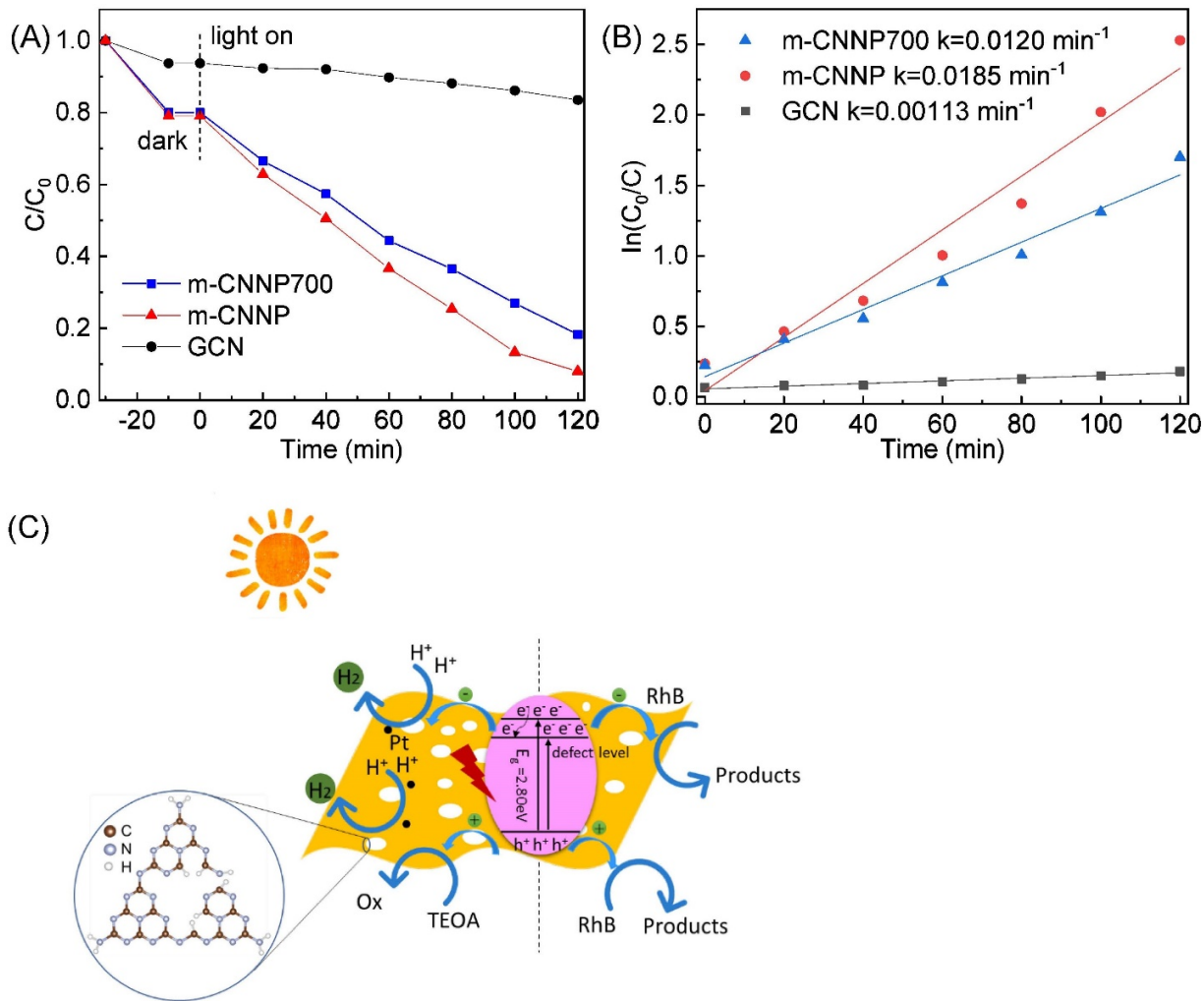


Fig. 10 (A) Photodegradation of RhB and (B) the relevant kinetic rate constants (K) calculation for GCN, m-CNNP and m-CNNP700. (C) Schematic illustration for the photocatalytic activities by m-CNNP700.